Phys. Med. Biol. **45** (2000) 1423–1435. Printed in the UK PII: S0031-9155(00)06502-7

New real-time strain imaging concepts using diagnostic ultrasound

A Pesavento†, A Lorenz†, S Siebers‡ and H Ermert‡

† Lorenz & Pesavento IT, Postfach 25 04 01, 44742 Bochum, Germany

‡ Department of Electrical Engineering, Ruhr-University Bochum, 44780 Bochum, Germany

E-mail: lp@lp-it.de (A Pesavento)

Received 30 July 1999, in final form 1 February 2000

Abstract. Two real-time strain imaging concepts and systems are presented. Both systems are based on a conventional ultrasound scanner that is connected to a PC with an A/D converter card for real-time data acquisition of rf data. Differential strain between successively acquired rf frames are estimated using phase root seeking. The first concept uses a special real-time implementation of manual elastography. In the second concept, denoted 'vibrography', the static compression is replaced by low-frequency axial vibration of the probe, still operating in quasistatic acquisition mode. The properties of both concepts are discussed with regard to noise and motion artefacts, and it is shown, using simulations and phantom experiments, that both imaging concepts yield the same kind of strain images. Vibrography has the advantage that no manual compression has to be applied, total compression can be very low and some motion artefacts are better suppressed.

1. Introduction

In the past, two different concepts for imaging the elasticity have been proposed. In the early 1990s a technique called elastography was described by Ophir *et al* (1991). With this technique the tissue is compressed and the tissue strain resulting from this compression is imaged. Since its invention this concept has been proposed for elasticity imaging of a wide range of different applications, including the prostate (Lorenz *et al* 1998, 1999), the breast (Krüger *et al* 1998, Garra *et al* 1997) and IVUS (Céspedes *et al* 1997). Another elasticity imaging concept is sonoelasticity imaging (Lerner *et al* 1990, Gao *et al* 1995), where the amplitude of motion produced by propagating low-frequency shear-waves is imaged using a technique which is similar to conventional Doppler. In this technique, information about the elastic tissue properties is derived from the Doppler signal.

The method of static strain imaging, i.e. elastography, has been adapted by many groups for different applications. The most promising concept, however, suffers from some disadvantages: first of all, since its invention elastography has been an off-line technique. Furthermore, relatively large compressions of the tissue are needed in comparison to the small vibration amplitudes used in sonoelasticity imaging.

We have recently proposed a new system for real-time strain imaging (Pesavento *et al* 1999b). The strain estimation concept introduced with this system is similar to the method proposed by Ophir *et al*. In this paper we discuss in detail the strain estimation concept used for this system, particularly its real-time properties, and extend the real-time concept to the use of a low-frequency, low-amplitude axial vibration instead of using static axial compression.

0031-9155/00/061423+13$30.00

The system set-up of the real-time system containing a conventional US (ultrasound) scanner and a PC for realtime strain estimation is explained in section 2. In section 3 the signal models for conventional real-time strain imaging and the new vibrography concept are derived. The digital signal processing strategies are explained in section 4, including the phase root seeking algorithm for fast and accurate strain estimation (Pesavento and Ermert 1998). In sections 5 and 6 the performance of both concepts with regard to noise and motion artefacts is compared.

2. System set-up

The developed real-time system uses a conventional US scanner (Kretz Combison 330) and operates with two different transducers: a 7.5 MHz transrectal probe for prostate examination and a 7.5 MHz abdominal sector scanner. The rf data are directly sampled into the PC memory by a PCI digital acquisition card (GaGe^{TM} 6012) with a sampling frequency of 30 MHz and 12 bit resolution. The data acquisition is done independently from the CPU by the PCI acquisition card, hence it does not take any calculation time. Using the transrectal probe, every frame is acquired at 10 frames per second. Using the abdominal probe every second frame is acquired at 15 frames per second. Regions of interest of approximately 2.2 cm $\times$ 2.6 cm for the transrectal probe and 3.5 cm $\times$ 4.0 cm for the abdominal probe are selected for calculating strain images, that have a size of 88×92 pixels for the abdominal probe and 66×68 pixels for the transrectal probe. For this purpose the rf data of two successive frames in the PC memory are used as pre- and post-compression images. Strain images are displayed colour-coded or grey- scaled on the PC without scan conversion. The acquired rf data and the calculated strain images are stored in ring buffers for additional off-line processing. Limited by the memory of the Pentium^{TM} III 450 MHz desktop PC (128 MB RAM), the rf data of up to 150 frames and 520 strain images are stored in cine buffers.

Two modes of compression are used to produce tissue strains: a manual linear compression throughout the scanning procedure or low-frequency vibration using a vibrating transducer, still operating in quasistatic mode. Limited by the frame rate of strain imaging, vibration frequencies between 0.5 Hz and 5 Hz are currently used. In the following we denote the former mode 'static strain imaging' and the later mode 'vibrography'. The low-frequency vibration of the transducers is produced by a stepping motor with a fixed transducer. A hand-held applicator will be used in the future.

3. Signal models

Similar to the data model for flow estimation, we use the terms 'slow time, fast time' throughout this paper. The time axis origin of the fast time t is reset each time the transducer fires. Hence the fast time variable denotes the time of flight and corresponds to the depth dependence of the echo signals. The slow time domain is denoted with capital letters. T is used to describe time-dependent variations in both rf frames and strain images. Likewise, the slow time frequency domain variables are denoted with capital letters (e.g. Ω) and fast time frequency domain variables are denoted with small letters (e.g. ω). Since very low-frequency vibrations and very slow compressions are used, the quasistatic assumption holds: the moment, at which a specific A-line is imaged, described by a slow time T_0 is assumed to be constant through the entire A-line, neglecting the fact that the deeper parts of the A-line are imaged later due to the time-of-flight of the excited ultrasonic pulse. A compression leads to the following rf echo data:

$$x(t, T) = x'\left(t + \int_{t'=0}^{t} \epsilon(t, T)\, \mathrm{d}t'\right) \tag{1}$$

where $x'(t)$ is the echo data of the examined tissue recorded at slow time T, without vibration, and $\epsilon(t, T)$ is the slow time-dependent strain inside the tissue due to the applied vibration. Its fast time dependence is due to its spatial variation. Assuming a mechanically linear medium and a reversible sinusoidal compression of the tissue with the frequency Ω_v, this strain can be modelled as follows:

$$\epsilon_v(t, T) = \epsilon_E(t) \cos(\Omega_v T). \tag{2}$$

The slow time dependence of $\epsilon_v(t)$ is due to its spatial variation. In comparison to (2), for static strain imaging, the linearly increasing applied strain leads to a spatially varying strain of

$$\epsilon_s(t, T) = \epsilon_0(t) T. \tag{3}$$

Echo data are acquired at a constant frame rate $1/\Delta T$ yielding

$$x_m(t) = x(t, m\Delta T) \tag{4}$$

where m denotes the index of the frame.

4. Real-time strain estimation

A signal processing algorithm for strain estimation should reconstruct the amplitude $\epsilon_E(t)$ of the slow time-dependent strain $\epsilon_v(t, T)$ in vibrography or the speed of compression $\epsilon_0(t)$ in static strain imaging. Again, note that the fast time dependence expresses depth dependence. Real-time strain estimation can be divided into the following parts: estimation of differential strain images $\epsilon_m(t)$ and estimation of $\epsilon_E(t)$ or $\epsilon_0(t)$ from differential strain images. Differential strain images $\epsilon_m(t)$ are defined by

$$\epsilon_m(t) = \epsilon(t, m\Delta T) - \epsilon(t, (m-1)\Delta T). \tag{5}$$

They can be estimated from two successively acquired rf data items $x_{m-1}(t)$ and $x_m(t)$. Differential strain images $\epsilon_m(t)$ can be considered as a sampled and filtered version of $\epsilon(t, T)$. The estimation of the differential strain is the most time-consuming part of strain estimation. Therefore axial displacements between $x_{m-1}(t)$ and $x_m(t)$ are estimated using the phase root seeking technique (Pesavento and Ermert 1998, Pesavento *et al* 1999a, b). This algorithm is a fast alternative to the widely used cross-correlation method. It is more accurate than other fast techniques, like curve-fitting methods (de Jong *et al* 1990). To estimate subsample time-shifts, the echo data are interpolated by a linear interpolation of the corresponding baseband signals (Pesavento *et al* 1999a). Interpolation is important for the estimation of subsample time shifts with high accuracy. In contrast to the search of the maximum of the cross-correlation function, phase root seeking finds the root of the phase of the correlation function of the analytic echo signals by a Newton iteration approach. After a small number of iterations (usually two to three), the algorithm converges. Note that in contrast to other concepts for displacement estimation that are evaluating the phase, including those used in Doppler imaging or sonoelasticity imaging, this concept does not rely on narrow-band signal characteristics. In fact, as is shown later, the accuracy of phase root seeking and other correlation techniques increases with increasing signal bandwidth.

Similar to the work of Ophir *et al* (1991), time shifts are estimated using a discrete number of windows at discrete depths. The time shift $\tau_{m,k}$ of the kth window of two A-lines centred around $t_k = k\Delta T$ is estimated by the following iterative formula:

$$\tau_{m,k,0} = \tau_{m,k-1,L}$$

$$\tau_{m,k,l} = \tau_{m,k,l-1} + \frac{1}{\omega_0} \arg\left(\exp(-\mathrm{j}\omega_0 \tau_{m,k,l-1}) \int_{t_k - T_w/2}^{t_k + T_w/2} b_m^*(t) b_{m+1}(t - \tau_{m,k,l-1})\, \mathrm{d}t \right) \tag{6}$$

where $b_m(t)$ denotes the baseband data of $x_m(t)$, and l is an iteration index. $L = 2$ iterations are used in this system. The quantity ω_0 denotes the nominal centre frequency of the transducer. T_w denotes the window length. Aliasing of the arg function in equation (6) can be successfully avoided if the difference of the time delays of two successive windows is smaller than π/ω_0, which is usually valid for small transducer motion.

When applying equation (6) to digital signals the integral is replaced by a sum. Furthermore, the post-compression signal has to be time shifted by a subsample time shift (Céspedes *et al* 1995). This is done using linear interpolation of baseband signals. Hence subsample time-shifts can be estimated. Baseband data $b_m(t)$ are obtained from the real-value rf data in two steps directly after the data acquisition:

(a) The complex analytic signal $a_m(t)$ is calculated by adding an imaginary part to the signal, which is equal to its Hilbert transform. The Hilbert transform is calculated using a 14-point FIR filter, designed by the signal processing toolbox of MATLAB™.
(b) To obtain the baseband signal, the analytic signal is multiplied by

$$b_m(t) = a_m(t)\exp(-\mathrm{j}\omega_0 t). \tag{7}$$

The windows for the time-shift estimation have a length of 0.93 μs (28 samples). Window overlaps of 50% are used. The differential strain $s_m(t)$ is estimated from the displacements by a least-square estimator (Kallel and Ophir 1997) using nine displacements for strain estimation.

The result, as given in equation (5), can be considered as a sampled and filtered version of strain $\epsilon(t, T)$. To reconstruct the quantity of interest $\epsilon_E(t)$ in the case of a vibrating transducer, two steps have to be performed:

(a) To separate the excited frequency Ω_v component from broadband noise components due to rf noise and motion artefacts, $\epsilon_m(t)$ has to be filtered using a narrow-band filter.
(b) The envelope has to be detected for the reconstruction of $\epsilon_E(t)$.

The latter task can be performed by calculating the absolute value of the analytic signal (analytic in terms of slow time T) of $\epsilon(t, T)$. The analytic signal $\tilde{\epsilon}_m(t)$ which is denoted 'analytic strain images' throughout this paper, can also be obtained by filtering. Hence all three parts, the reconstruction of $\epsilon(t, T)$ from differential strains $\epsilon_m(t)$ described by equation (5), the narrow band filtering operation for the separation of the frequency Ω_v and finally the calculation of the analytic strain images can be performed by the implementation of the slow time filter function

$$H(\Omega) = \frac{2}{1 - \exp(-\mathrm{j}\Omega_v \Delta T)}\delta(\Omega - \Omega_v). \tag{8}$$

This filter function directly reconstructs the analytic strain images $\tilde{\epsilon}_m(t)$ from the differential strain images $\epsilon_m(t)$. The first part of the filter inverts the filtering introduced by equation (5). The analytic signal is calculated by suppressing negative frequency components. In a real-time system, a digital implementation using low-order filters is preferred. A first-order approximation of the filter described by (8) can be described by the following differential equation

$$\tilde{\epsilon}_m(t) = k[\epsilon_m(t) - p\exp(-\mathrm{j}\Omega_v \Delta T)\epsilon_{m-1}(t)] - p\exp(\mathrm{j}\Omega_v \Delta T)\tilde{\epsilon}_{m-1}(t) \tag{9}$$

with

$$k = 2\left|\frac{1-p}{[1 - \exp(-\mathrm{j}\Omega_v \Delta T)][1 - p\exp(-2\mathrm{j}\Omega_v \Delta T)]}\right|. \tag{10}$$

The filter is a first-order complex FIR filter cascaded by a first-order complex recursive filter. The frequency response of the filter is presented in figure 1 (left) for $\Omega_v \Delta T = 0.5$ and

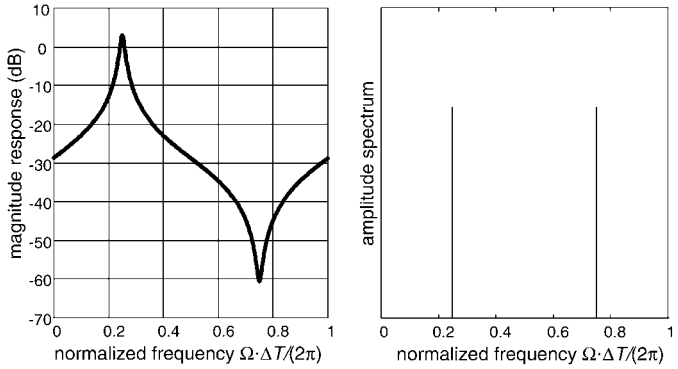

Figure 1. Amplitude spectrum of a sinusoidal vibration (right) and frequency response of the filter (left) for the reconstruction of the corresponding analytic signal.

$p = 0.95$. Figure 1 (right) shows a sketch of the amplitude spectrum of the vibration, which has two delta peaks, at $\pm\Omega_\nu$. The filter described by equation (9) has been designed such that the delta peak at $-\Omega_\nu$ is effectively suppressed.

In case of static strain imaging, a similar filter is used for the reconstruction of $\epsilon_0(t)$:

$$\bar{\epsilon}_m(t) = \frac{1-p}{\Delta T}\epsilon_m(t) - p\bar{\epsilon}_{m-1}(t). \tag{11}$$

$\bar{\epsilon}_m(t)$ is a real valued function, which is an estimator for $\epsilon_0(t)$ in equation (3). Nevertheless, we take the absolute value of $\epsilon_0(t)$. Consequently, compressing the tissue or releasing it results in the same strain images. With the filter described in equation (11), a noise reduction is achieved by a recursive filtering of the strain images, which is similar to the multicompression approach proposed by O'Donnell *et al* (1993). Here several successive strain images are averaged, which can be mathematically described by a temporal FIR filter in a real-time system. Noise is reduced at the expense of temporal resolution with regard to the slow time. With $p = 0$ no filtering is applied.

5. Noise performance

There are two major sources of noise in strain imaging: noise on rf data and decorrelation noise caused by transverse tissue motion and speckle decorrelation. Decorrelation may result from the applied compression or other motion sources. Its amount is closely related to the correlation coefficient of pre- and post-compression images. Hence, in a real-time system, where lateral motion tracking algorithms cannot be performed due to their computational complexity, decorrelation noise is rather a technical problem: in order to obtain high correlations between pre- and post- compression images, the differential strain has to be small, which means that either the applied strain has to be low or its has to be tracked very fast using high frame rates $1/\Delta T$, which is a technical demand. In a real-time system, however, the user has an immediate feedback and the amount of applied strain can be adjusted such that decorrelation noise is minimized, but this is easier in a system with a high-frame rate.

In this section we focus on the influence of rf noise, since this noise is significantly influenced by the applied filters in both vibrography and static strain imaging and determines the lower bound of noise in the strain images. To obtain the stochastic properties of the noise of the strain estimation, simulations have been performed in order to investigate the slow time behaviour of the noise on differential strain images, which serve as the input for the filters in

both vibrography and static strain imaging. The slow time behaviour can be described by the autocovariance function, which describes variance and correlation of the noise of two arbitrary differential strain images $\varepsilon_m(t)$ and $\varepsilon_n(t)$.

For the simulation, echo signals were simulated as described in Pesavento *et al* (1999a). The echo signals have a Gaussian power spectrum with a centre frequency of 7.5 MHz and a relative bandwidth of 66%. The sampling frequency is 30 MHz. Noise with a rectangular spectrum within the transducer's bandwidth was added to the signals leading to SNR ranging from 10 dB to 30 dB. The differential strain between two images was chosen to be less than 0.5%.

It can be shown that the normalized autocorrelation function, which can be obtained by normalizing the autocovariance function to its variance, can be approximated by

$$c(\Delta, m) = \operatorname{corr}(\epsilon_m(t), \epsilon_{m+\Delta m}(t)) = \begin{cases} 1 & \text{for } \Delta m = 0 \\ -0.5 & \text{for } |\Delta m| = 1 \\ 0 & \text{for } |\Delta m| > 1. \end{cases} \tag{12}$$

The same autocorrelation function is obtained when filtering white noise with a filter described by equation (5).

The variance of the strain can be compared to its theoretical lower bound, the Cramer–Rao lower bound (CRLB). Expressions for the CRLB for strain estimation have been derived in Schultheiss and Weinstein (1979) and Friedlander (1984):

$$\sigma_\epsilon^2 \geqslant \frac{24\pi}{T_G^3} \left\{ \int_0^\infty \frac{2\omega^2 C_{XX}^2(\omega)/_{NN}^2(\omega)}{1 + 2C_{XX}(\omega)/C_{NN}(\omega)} \, \mathrm{d}\omega \right\}^{-1}. \tag{13}$$

In this expression, T_G denotes the total observation time used for the estimation of a differential strain value. T_G is determined by both the window length T_W used for time delay estimation and the order of the least-squares estimator used for the estimation of strain from time delays. $C_{XX}(\omega)$ denotes the power spectrum of the echo-signals and $C_{NN}(\omega)$ denotes the noise spectrum. For rectangular spectra, this expression approximately reduces to

$$\sigma_\epsilon^2 \geqslant \frac{3}{T_G^3 \pi^3 f_0^2 B \mathrm{SNR} \omega_0} \tag{14}$$

where B denotes the bandwidth and SNR denotes the signal to noise ratio $C_{XX}(\omega)/C_{NN}(\omega)$. Figure 2 compares the mean square error of strain estimation to its CRLB for differential strains. The simulation has been performed using strains of 0.25% and 1%. The signal-to-noise ratio of the echo data was adjusted to 20 dB. This figure shows that using the estimator for differential strains described above, the CRLB can almost be reached for low strains. The window length T_W, used for the generation of this figure is $T_W = 0.53\ \mu$s. The windows used for time-delay estimation have an overlap of 75%.

The power spectrum of the noise on differential strain images can be derived from the covariance function:

$$C_{\epsilon\epsilon}(\Omega) = \frac{\sigma_\epsilon^2}{2} |1 - \exp(-\mathrm{j}\Omega \Delta T)|^2. \tag{15}$$

Again σ_ϵ^2 denotes the variance of differential strain images. The filter described by equation (9) leads to the power spectrum of the analytic strain:

$$C_{\tilde{\epsilon}\tilde{\epsilon}}(\Omega) = \frac{|k|^2 \sigma_\epsilon^2 |1 - \exp(-\mathrm{j}\Omega\Delta T)|^2 |1 - p \exp[-\mathrm{j}(\Omega + \Omega_v)\Delta T]|^2}{2|1 - p \exp[-\mathrm{j}(\Omega - \Omega_v)\Delta T]|^2}. \tag{16}$$

Hence

$$C_{\tilde{\epsilon}\tilde{\epsilon}}(\Omega_v) = 2\sigma_\epsilon^2. \tag{17}$$

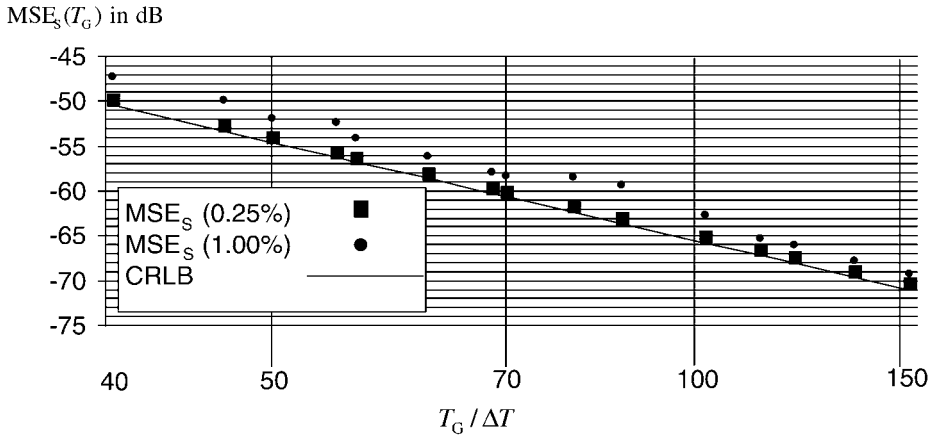

Figure 2. Comparison of the mean square error of the differential strain estimation to its Cramer–Rao lower bound as a function of observation length for 0.25% strain and 1.0% strain.

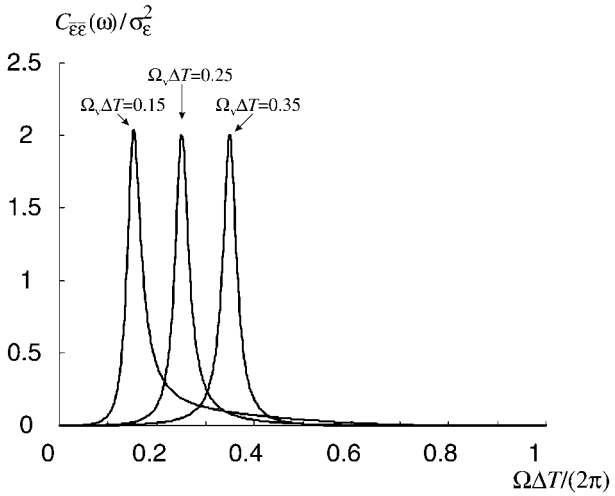

Figure 3. Power spectra of the noise on the analytic signal due to rf noise after filtering for different vibration frequencies.

In figure 3 three examples are plotted for the power spectrum for $\Omega_\nu \Delta T/2\pi = 0.15$, $\Omega_\nu \Delta T/2\pi = 0.25$ and $\Omega_\nu \Delta T/2\pi = 0.35$. It can be noticed that the shape of the power spectrum is relatively independent of $\Omega_\nu \Delta T$, except for $\Omega_\nu \Delta T \to 0$ or $\Omega_\nu \Delta T \to \pi$. The variance of the noise can be found by combining equations (5) and (9) to give

$$\sigma_{\bar{\epsilon}}^2 = 2\sigma_\epsilon^2 \frac{1-p}{1+p} \frac{1 + p^2[1 - 2\cos(2\Omega_\nu \Delta T)] + p^3[\cos(3\Omega_\nu \Delta T) - \cos(\Omega_\nu \Delta T)]}{[1 - \cos(\Omega_\nu \Delta T)][1 + p^2 - 2p\cos(2\Omega_\nu \Delta T)]}. \tag{18}$$

Figure 4 shows this variance as a function of Ω_ν for different p. For large values of p, the variance is almost constant in a wide range of Ω_ν, $\Omega_\nu = 0.3/\Delta T$ is, however, always a good choice. In this case the variance can be approximated by

$$\sigma_{\bar{\epsilon}}^2 \approx \sigma_\epsilon^2 (1 - p). \tag{19}$$

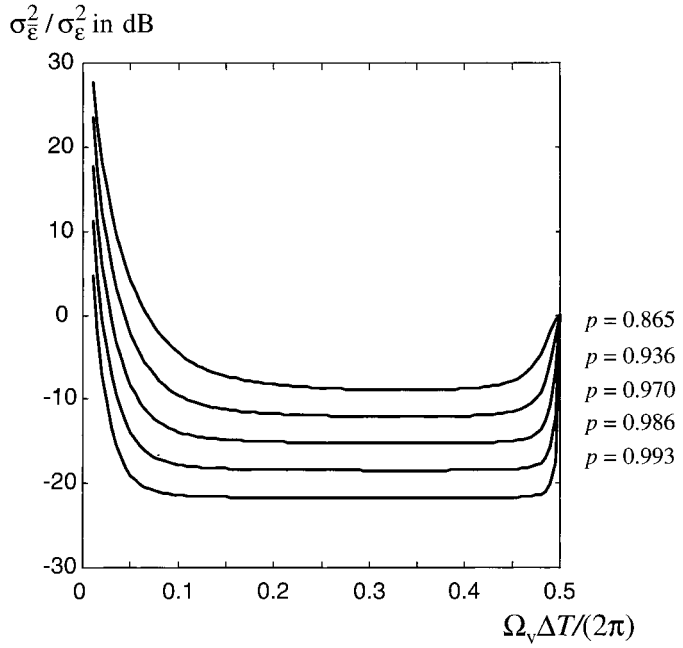

Figure 4. Variance of the noise on the analytic signal due to rf noise after filtering as a function of vibration frequency. The variance is normalized to the variance of single differential strain images (input of the filter).

In the case of static strain imaging, the noise power spectrum is

$$C_{\bar{\epsilon}\bar{\epsilon}}(\Omega) = \sigma_\epsilon^2 \frac{(1-p)^2}{\Delta T^2} \frac{1-\cos(\Omega \Delta T)}{1+p^2-2p\cos(\Omega \Delta T)} \tag{20}$$

and the variance is

$$\sigma_{\bar{\epsilon}}^2 = \sigma_\epsilon^2 \frac{(1-p)^2}{\Delta T^2(1+p)} \approx \frac{\sigma_\epsilon^2 (1-p)^2}{2\Delta T^2}. \tag{21}$$

In both cases, static strain imaging and vibrography, the time T_H until the brightness of an image pixel reaches half of its maximum value after a compression with constant $\epsilon_0(t)$ or constant vibration amplitude $\epsilon_E(t)$ has been applied, depends in the same way on p and ΔT:

$$T_H = \Delta T \frac{\ln(0.5)}{\ln(p)} \approx 0.693 \frac{\Delta T}{1-p}. \tag{22}$$

This time, which we refer to as the 'half-life period', can be considered as a measure of integration time, during which differential strain images are averaged by the filters described in equations (9) or (11).

A comparison of the noise performance of static strain imaging and vibrography is difficult, since the constraints, which limit the amounts of applied strains, are different. In both cases, unless the differential strain exceeds certain limits, the generated noise is independent of the applied strain. Hence the signal-to-noise ratio can be increased by increasing the amount of applied strain, i.e. the speed of the linearly increasing strain $\epsilon_0(t)$ in static strain imaging or the amplitude $\epsilon_E(t)$ of the vibration in vibrography.

However, this increase is limited by different constraints: in both cases the differential strain should not significantly exceed 0.5–1%. Larger differential strains increase decorrelation

Table 1. Noise performances of vibrography and static strain imaging as a function of the signal-to-noise differential strain image.

	SNR	Total strain	$S(t, T)$
Static strain imaging	$\mathrm{SNR}_\epsilon(\Delta\epsilon)\frac{T_H^2}{(0.693\Delta T)^2}$	$\frac{T_H}{\Delta T}\Delta\epsilon$	$\frac{\Delta\epsilon}{\Delta T}T$
Vibrography	$\mathrm{SNR}_\epsilon(\Delta\epsilon)\frac{T_H}{0.693\Delta T}$	$2\Delta\epsilon$	$\Delta\epsilon\cos\left(\frac{0.3T}{\Delta T}\right)$

noise. This is the only constraint in vibrography. In static strain imaging other considerations have to be taken into account: first, the total applied strain may be limited due to physiological reasons. This is a limitation for ϵ_0, since a linear increase has to be kept constant at least during the settling time of the recursive filter, which may result in large total strains. Second, the averaging of strain images during large total compressions in static strain imaging may be inaccurate due to large displacements. Decorrelation effects can be reduced by increasing the frame rate $1/\Delta T$ of real-time differential strain imaging. The half-life period T_H can be kept constant during this increase of the frame rate, by adjusting p according to equation (22).

In table 1 the noise performance of both vibrography and static strain imaging are compared under the following assumption: the applied strain is chosen such that the slow temporal means $\Delta\epsilon$ of the absolute value of the differential strains are equal, e.g. 0.5%. This leads to a signal-to-noise ratio SNR_ϵ of a single differential strain image. Table 1 shows how the signal-to-noise ratios of vibrography and static strain imaging are related in respect this to SNR_ϵ. In addition, the total applied strain during the half-life period T_H is shown. In these formulae T_H and the inverse of the frame rate ΔT are used as parameters. The constant p is implicitly given by equation (22) and Ω_v was set to $0.3/\Delta T$.

The quotient $T_H/\Delta T$ can be considered as a measure of the number of averaged strain images. Table 1 shows the following: the merit of the averaging is higher for static strain imaging, since the SNR is proportional to the square of the half-life period or the number of averaged strain images. In vibrography, the SNR is proportional to the half-life period or the number of averaged strain images. However, in static strain imaging, this gain in SNR is only achieved by a higher total strain than for a single differential strain image, whereas in vibrography the gain in SNR is achieved by an averaging of repeatedly acquired differential strain images. For fixed, but relatively large, ΔT, static strain imaging may be preferred, since the total strain has to be low anyway to avoid decorrelation. However, application of slow continuously increasing strain poses some technical problems. For small ΔT, vibrography can reach high SNR without significant total strain.

Note, that if the total strain or the strain velocity ϵ_0 is to be kept fixed the SNR cannot be increased by increasing the frame rate in static strain imaging. In this case, increasing the frame rate results in a decrease of $\Delta\epsilon$, and SNR_s is proportional to $\Delta\epsilon^2$.

In vibrography this is the case, since the number of averaged strain images is increased through an increase of Ω_v. Total strain is always constant for vibrography, when changing the frame rate.

5.1. Motion artefacts

Table 2 shows the resulting SNR after filtering for $1/\Delta T = 7.5$ Hz, $1/\Delta T = 15$ Hz and $T_H = 0.8$ s. The fundamental frequency of the periodic triangular motion was assumed to be 1 Hz for blood flow and 0.2 Hz for respiration. Table 2 shows that the SNR of vibrography is between 10 and 20 dB better than the values for static strain imaging with respect to the suppressions of motion artefacts.

Table 2. Comparison of signal-to-noise ratios concerning strain noise generated by a low-frequency vibrating tissue motion for both vibrography and static strain imaging.

	$1/\Delta T = 7.5$ Hz		$1/\Delta T = 15$ Hz	
	Respiration	Blood flow	Respiration	Blood flow
Static strain imaging	−38.3 dB	−41.0 dB	−38.1 dB	−39.7 dB
Vibrography	−22.6 dB	−31.5 dB	−16.3 dB	−24.7 dB

Strain images can be corrupted by motion artefacts, caused by motion inside the tissue itself. One problem is the increase of decorrelation noise due to these kinds of motion. This problem can be reduced by the use of high frame rates, i.e. small ΔT, which ensures coherence between pre- and post-compression images. Another problem is the presence of differential strains which are caused by tissue motion itself. This tissue motion is correctly measured by the displacement estimation; however, it is superimposed on strains which are caused by the applied compressions. Differential strain images are created from displacement images by filtering along the fast time axis. Hence differential strain images have the same slow time behaviour as displacement images and thus the tissue motion itself. In this paper we consider two cases: in a general-purpose approach, the tissue motion is regarded to be white noise with respect to its slow time behaviour. This is a reasonable approach for motion caused by any unknown source, e.g. muscle motion or motion of the patient. In this case, the power spectrum of the noise introduced into the differential strain images can be described by equation (15) and hence it possesses the same slow time behaviour as noise created by rf noise. The influence of the described filters is summarized in table 1. In cases in which tissue motion caused by the blood flow or respiration is the main source of motion artefacts, the resulting noise has an almost periodic slow time behaviour. The fundamental frequency is about 1 Hz for blood flow and 0.1–0.2 Hz for respiratory motion. Those are relatively low frequencies compared to typical vibration frequencies between 2–3 Hz applied for our system, which has a frame rate of $1/\Delta T = 7.5$ Hz. Consequently, these motions are better suppressed by the filters used in vibrography in comparison to static strain imaging. To show this, the influence of a triangular periodic motion on the strain signal-to-noise ratio was analysed using simulations. In these simulations a sinusoidal vibration is superposed by a periodic triangular motion and filtered by (9) or (11). With these simulations the performances of vibrography and static strain imaging for the suppression of the periodic triangular motion are compared. Since we are only interested in a direct comparison of the two methods, motions of an arbitrary amplitude may be chosen. The amplitude of the applied compressions and the amplitude of the triangular motion was chosen such that the average resulting differential strain of each component equals $\Delta\epsilon$.

6. Phantom studies

To demonstrate the described properties of the two methods, a phantom has been constructed which consists of a sponge in which hard lesions have been included by injecting a 3% agar-agar solution. The hard lesions is about 10 times stiffer than the surrounding sponge. Figure 5 shows typical strain images obtained using the static strain imaging concept with manual application of the compression using a hand-held transducer. The strain is displayed by grey-scale map. Bright regions denote high strain, dark regions low strain. In the electronic version of the paper, a colour coded video sequence is supplied to demonstrate the real-time behaviour. The images shows the typical strain patterns around a hard lesion, simulated by FEM methods by

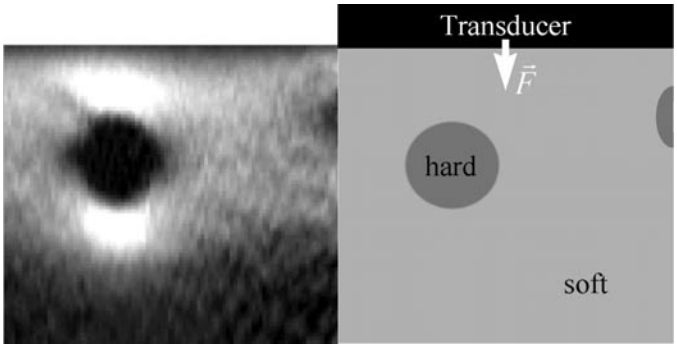

Figure 5. Strain image of a hard inclusion in a soft sponge obtained in real-time using the static strain imaging concept.

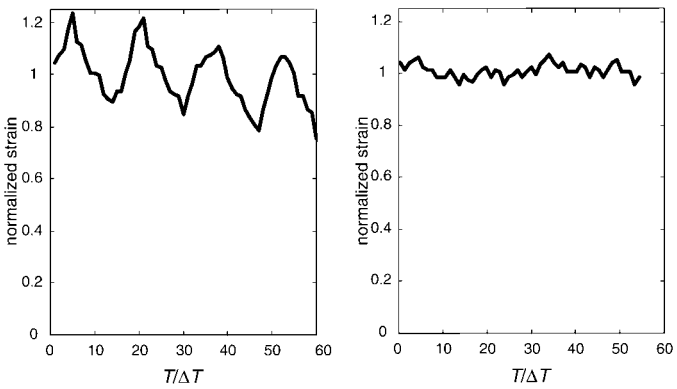

Figure 6. Normalized strain at a single image pixel versus slow time in the presence of a periodic unwanted tissue motion of static strain imaging (left) and vibrography (right).

many authors (e.g. Chaturvedi *et al* 1998). The low SNR in the lower right and lower left regions of the image are due to decorrelation noise caused by the use of a sector probe (Lorenz *et al* 1998).

The influence of tissue motion is demonstrated in figure 6. The same cross section through a hard lesion was imaged using the vibrography and the static strain imaging concept. A defined strain was automatically applied using a stepping motor. In both cases, a 0.25 Hz periodic triangular motion was superposed. This vibration simulates respiratory motion. In vibrography, the vibration also was a periodic triangular motion of 2.25 Hz. The amplitude of the strain in vibrography and the velocity of the increasing compression in static strain imaging was chosen such that the means of the differential compression was 0.2 mm, which corresponds to an average differential compression of approximately 0.4% between two images or 3% per second for static strain imaging. The 0.25 Hz vibration that simulates respiratory motion has the same amplitude. In both cases T_H was equal to 0.8 s. The low-frequency vibration led to low-frequency vibrations in the resulting strain images. Note, however that *in vivo* the source of unwanted motion may be inside the imaged tissue and result in spatially varying motion artefacts. Furthermore, in this case the amplitude of strain produced by the unwanted tissue motion depends not only on the displacement but also on its spatial distribution. Hence the presented experiment demonstrates only the slow time behaviour of motion artefacts. In figure 6

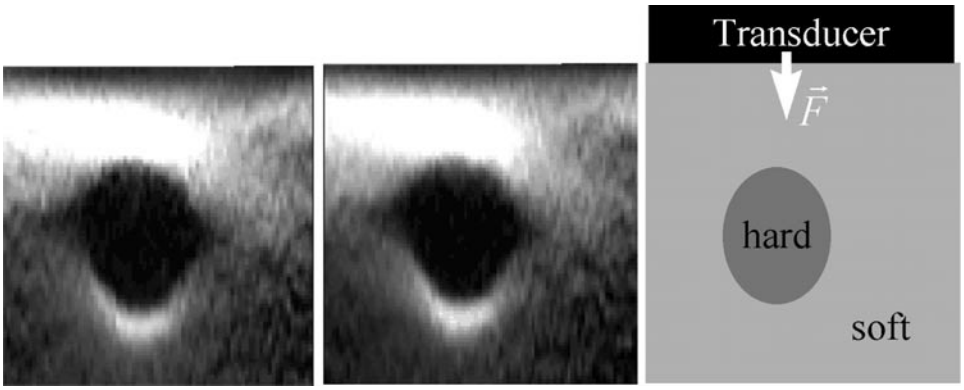

Figure 7. Comparison of strain images of a hard inclusion obtained in real-time using vibrography (left) and the static strain imaging concept (right).

the slow time variation of one image point is plotted against the slow time for both vibrography and static strain imaging. As expected from the above simulations, for static strain imaging the variation is much larger. Furthermore, there is a noticeable decay of the mean value for the plot obtained with static strain imaging. This is due to the slowly changing location of the image region that is observed by a specific image point with increasing compression.

Figure 7 compares two single images and demonstrates the equivalence of the strain images for both techniques. In the electronic version of the paper, movies of the strain images are supplied.

In this phantom experiment, the speed at which the compression was applied is relatively large. However, the experiment shows that total compression of the order of 10% are not uncommon in order to obtain a stable image for a few seconds.

7. Conclusion

In this paper, two real-time strain imaging concepts have been introduced and compared. Simulations and *in vitro* studies on phantoms show that real-time strain images can be calculated using a conventional desktop PCs. A major disadvantage of static strain imaging concepts in some applications is that high compressions are necessary in order to obtain high-strain SNR. This problem is more severe for real-time strain imaging, where longer periods of constantly increasing compressions are necessary in order to obtain stable strain images for a longer time. Vibrography overcomes this disadvantage by applying low-frequency vibrations (0.1–20 Hz, depending on the frame rate $1/\Delta T$). We have shown that the resulting strain images are equivalent to conventional strain images. With this technique, high-SNR real-time strain images which are stable over an infinite duration can be obtained with very low total compressions which are of the order of 0.1%.

The noise performance of both concepts has been compared and shown to be different. In both concepts increasing the frame rate at which differential strain images are acquired will significantly increase the strain SNR, but in static strain imaging the speed of compression has to be increased correspondingly in order to increase the SNR, which is limited by practical or physiological reasons. Another argument for high frame rates is the fact that the coherence between the rf frames is increased and thus decorrelation noise is decreased. Unwanted motion of the tissue, e.g. vessel motion or respiratory motion, causes decorrelation of successive

frames, but also strain artefacts due to the resulting, properly estimated, displacements. These artefacts can better be suppressed using the technique of vibrography.

References

Céspedes E I, de Korte C L and van der Steen A F W 1997 Intravascular ultrasonic palpation: assessment of local wall compliance *Proc. 1997 IEEE Ultrasonic Symp.* pp 1079–82

Céspedes E I, Huang Y, Ophir J and Spratt S 1995 Methods for the estimation of subsample time delays of digitized echo signals *Ultrason. Imaging* **17** 142–71

Chaturvedi P, Insana M F and Hall T J 1998 2-D Companding for noise reduction in strain imaging *IEEE Trans. Ultrason. Ferroelectr. Freq. Control* **45** 179–91

de Jong P G M, Arts T, Hoeks A P G and Renemann R S 1990 Determination of time motion velocity by correlation interpolation of pulsed ultrasonic echo signals *Ultrason. Imaging* **12** 84–98

Friedlander B 1984 On the Cramer–Rao bound for time delay and doppler estimation *IEEE Trans. Inform. Theory* **30** 575–80

Gao L, Parker K J and Alam S K 1995 Sonoelasticity imaging: theory and experimental verification *J. Acoust. Soc. Am.* **97** 3875–86

Garra B S, Céspedes E I, Ophir J, Spratt S R, Zuurbier R A, Magnant C M and Pennanen M F 1997 Elastography of breast lesions: initial clinical results *Radiology* **202** 79–86

Kallel F and Ophir J 1997 A least-square estimator for elastography *Ultrason. Imaging* **19** 195–208

Krüger M, Pesavento A, Ermert H, Hiltawsky K M, Heuser L and Jensen H R A 1998 Ultrasonic strain imaging of the female breast using phase root seeking and three-dimensional optical flow *Proc. 1998 IEEE Ultrasonic Symp.* pp 1757–60

Lerner R M, Huang S R and Parker K J 1990 Sonoelasticity images derived from ultrasound signals in mechanically vibrated tissues *Ultrasound Med. Biol.* **16** 231–9

Lorenz A, Sommerfeld H, Garcia-Schürmann M, Philippou S, Senge T and Ermert H 1999 A new system for the acquisition of ultrasonic multicompression strain images of the human prostate *in vivo IEEE Trans. Ultrason. Ferroelectr. Freq. Control* **46** 1147–54

Lorenz A, Sommerfeld H, Garcia-Schürmann M, Philippou S, Senge T, Philippou H E, Senge T and Ermert H 1998 Diagnosis of prostate carcinoma using multicompression strain imaging: data acquisition and first *in vivo* results *Proc. 1998 IEEE Ultrasonic Symp.* pp 1761–4

O'Donnell M, Emelianov S Y, Skovorda A R and Shapo S M 1993 Quantitative elasticity imaging *Proc. 1993 IEEE Ultrasonic Symp.* pp 893–903

Ophir J, Céspedes I, Ponnekanti H, Yazdi Y and Li X 1991 Elastography, a quantitative method for imaging the elasticity of biological tissues *Ultrason. Imaging* **13** 111–34

Pesavento A and Ermert H 1998 Time-efficient and exact algorithms for adaptive temporal stretching and 2D-correlation for elastographic imaging using phase information *Proc. 1998 IEEE Ultrasonic Symp.* pp 1765–8

Pesavento A, Lorenz A and Ermert H 1999b System for real-time elastography *Electron Lett.* **35** 941–2

Pesavento A, Perrey C, Krueger M and Ermert H 1999a A time efficient and accurate strain estimation concept for ultrasonic elastography using iterative phase zero estimation *IEEE Trans. Ultrason. Ferroelectr. Freq. Control* **46** 1057–67

Schultheiss P M and Weinstein E 1979 Estimation of differential Doppler shifts *J. Acoust. Soc. Am.* **66** 1412–19